Nonlinear Optical Response of a WS$_2$ Monolayer at Room Temperature upon Multicolor Laser Excitation

Hernandez-Rueda, Javier; Noordam, Marc L.; Komen, Irina; Kuipers, L.

Important note
To cite this publication, please use the final published version (if applicable).
Please check the document version above.

Article

Nonlinear Optical Response of a WS$_2$ Monolayer at Room Temperature upon Multicolor Laser Excitation

Javier Hernandez-Rueda, Marc L. Noordam, Irina Komen, and L. Kuipers*

Read Online

ACCESS | Metrics & More | Article Recommendations

ABSTRACT: Currently, the nonlinear optical properties of 2D materials are attracting the attention of an ever-increasing number of research groups due to their large potential for applications in a broad range of scientific disciplines. Here, we investigate the interplay between nonlinear photoluminescence (PL) and several degenerate and nondegenerate nonlinear optical processes of a WS$_2$ monolayer at room temperature. We illuminate the sample using two femtosecond laser pulses at frequencies ω_1 and ω_2 with photon energies below the optical bandgap. As a result, the sample emits light that shows characteristic spectral peaks of the second-harmonic generation, sum-frequency generation, and four-wave mixing. In addition, we find that both resonant and off-resonant nonlinear excitation via frequency mixing contributes to the (nonlinear) PL emission at the A-exciton frequency. The PL exhibits a clear correlation with the observed nonlinear effects, which we attribute to the generation of excitons via degenerate and nondegenerate multiphoton absorption. Our work illustrates a further step toward understanding the fundamental relation between parametric and nonparametric nondegenerate optical mechanisms in transition-metal dichalcogenides. In turn, such understanding has great potential to expand the range of applicability of nonlinear optical processes of 2D materials in different fields of science and technology, where nonlinear mechanisms are typically limited to degenerate processes.

KEYWORDS: nonlinear optics, four-wave mixing, sum-frequency generation, second-harmonic generation, exciton, transition-metal dichalcogenides
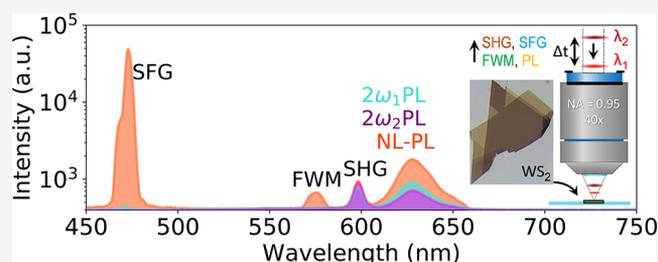
Today, atomically thin two-dimensional layered materials (2DLMs) are at the focus of the optics and photonics community due to their unique optical and electrical properties.[1−6] Therefore, this new generation of materials has led to a myriad of applications in science and nanotechnology, for instance, in the fields of nanophotonics and photovoltaics.[7−11] Recently, the nonlinear optical response of several 2DLMs has been reported to be remarkably large.[12,13] In particular, inversion symmetry breaking and efficient light–matter interaction make transition-metal dichalcogenides (TMDs) an ideal platform to investigate nonlinear optics.[14,15] Several second- and third-order nonlinear parametric mechanisms, generated during monochromatic laser illumination, have been observed in a wide variety of TMDs, including MoS$_2$,[16−22] MoSe$_2$,[23,24] MoTe$_2$,[25] WSe$_2$,[13,26] WS$_2$,[27,28] and ReS$_2$.[29] The study of nondegenerate parametric processes (i.e., involve several photon frequencies), such as sum-frequency generation (SFG) and four-wave mixing (FWM), is limited and has been shown in Mo-based[30−33] and W-based[34,35] TMDs.

All the above-mentioned nonlinear optical processes in TMDs open up an extraordinarily broad range of application perspectives within several research and technical disciplines; Autere et al. recently provided an exhaustive review.[15] For instance, the phase-sensitive nature of some parametric mechanisms has been utilized in nonlinear frequency conversion applications[17,36] as well as to accurately characterize the crystallographic properties of new 2D nanomaterials, exploring the influence of strain,[37] substrate,[38] defects, and neighboring grains.[39] In the field of biology, the good biocompatibility and reduced dimensionality of 2DLMs make them ideal candidates for noninvasive, nonlinear-based bioimaging solutions, yielding a superior spatial resolution, background-free signal, and large imaging depth.[40,41] However, the already extensive range of applications, where degenerate mechanisms are typically employed, would benefit from using nondegenerate nonlinear mechanisms. For example, in materials science and quantum technologies, FWM has been reported to provide a superior way of (i) characterizing the thickness of few-layered TMDs over second-order nonlinear

processes[22,30] and (ii) creating entangled photon pairs using carbon nanotube films.[42] Therefore, it is relevant to achieve a better fundamental understanding of the relationship between nondegenerate parametric and nonparametric optical mechanisms in TMDs.

To understand the above-mentioned relationship in semiconductors, it is crucial to consider the role of light-induced electron−hole pairs (i.e., excitons) in parametric processes and their effect on the nth-order nonlinear susceptibility $\chi^{(n)}(\omega)$. In the case of 2DLMs, it is more adequate to use the surface conductivity $\sigma^{(n)}$ to describe the nonlinear optical response by relating the sheet current $j^{(n)}(\omega)$ to the electric field $E(\omega)$, where $\sigma^{(n)}$ is a $(n + 1)^{\text{th}}$-rank tensor that depends strongly on the symmetry of the crystal structure of the medium and its composition. The contribution of light-induced excitons to the $\sigma^{(n)}$ of TMDs is particularly relevant, as resonances between the laser frequency and excitonic states favor certain multiphoton-based mechanisms. These resonances and the selection rules for one-photon and two-photon PL have been reported in systems with reduced dimensionality such as carbon nanotubes and TMD monolayers.[13,43] For TMD monolayers, the role of excitons is even more relevant than for their multilayer and bulk counterparts, as the Coulomb interaction between electrons and holes is enhanced due to the quantum confinement and the reduced dielectric screening inherent to an atomically thin system.[13] In turn, this enhancement leads to an increase of radiative transition probabilities and the implication of the presence of excitons on the nonlinear response of monolayers. Lafrentz et al. recently developed a microscopic theory to explain the role of the symmetries of the wave functions of excitons on the nonlinear optical response of ZnO.[44] Later, this theory was used to derive the second-order susceptibility that explains SHG at exciton resonances in WSe$_2$.[13] However, the generation of excitons via nondegenerate multiphoton absorption, its influence on the nonlinear response of TMD monolayers and on the PL emission has not been investigated yet.

In this Article, we report on the nonlinear optical response of a WS$_2$ monolayer upon two-color laser illumination and its relation with the nonlinearly generated exciton PL. We use multiphoton spectroscopy to measure the emission spectra that arise when exciting the sample at room temperature with laser pulses at two different wavelengths $\lambda_1 = 775$ nm and $\lambda_2 = 1200$ nm that are temporally and spatially overlapped, as shown in Figure 1a. We find a strong nonlinear response simultaneously identifying several parametric mechanisms, including SHG, SFG, and FWM, as well as nonparametric processes like nonlinear PL. On one hand, we demonstrate the contribution of both degenerate and nondegenerate multiphoton absorption to the generation of excitons that result in nonlinear PL emission. On the other hand, we observe an enhanced SHG signal around the A-exciton resonance that we explain using the surface conductivity tensor derived using perturbation theory. We discuss these observations taking into account the parametric and nonparametric nature of the involved mechanisms.

EXPERIMENTAL SECTION

Our sample consists of flakes of WS$_2$ on a thin glass substrate. We mechanically exfoliate commercially available bulk WS$_2$ (2D semiconductor) and transfer it onto the glass substrate using tape. The glass substrate is cleaned before the transfer process both using chemicals and oxygen plasma. The sample
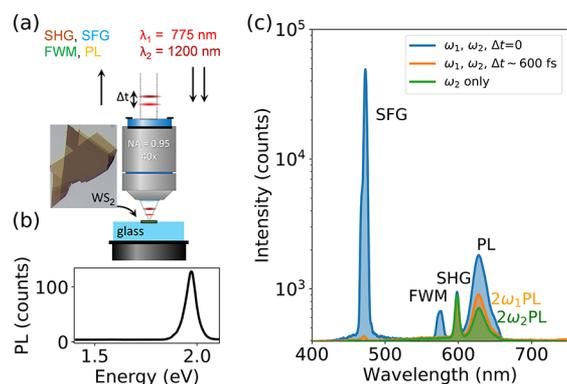
Figure 1. (a) Schematic of the experimental setup. Two laser beams at λ_1 and λ_2 are focused onto a WS$_2$ monolayer using an objective lens. The emitted light, including SHG, SFG, FWM, and PL, is collected by the same lens and detected using a spectrometer. (b) PL spectrum of the WS$_2$ monolayer. The PL shown here was generated using an excitation laser wavelength of 1180 nm. (c) Emission spectra acquired upon multiwavelength laser illumination and different time delays. The curves present the spectra collected upon illumination with ω_2-only (green), ω_1, and ω_2 with (blue, $\Delta t = 0$ fs) and without (orange, $\Delta t = 600$ fs) temporal overlap. The average power values of the beams at λ_1 and λ_2 were set to be 53 and 21 mW, respectively, at a repetition rate of 82 MHz and with a pulse duration of approximately 230 fs. The polarization angle of the beams is parallel with respect to each other and its angle with respect to the sample was optimized to maximize the FWM signal. The color labels on the right-hand side indicate the different multiphoton mechanisms that lead to PL, that is, two-photon absorption that leads to PL, $2\omega_1$PL, and $2\omega_2$PL.

is shortly heated at 100 °C before the removal of the tape (see also ref 6). We first inspect the sample using optical microscopy and then identify monolayers by recording their spectral signature with our multiphoton spectroscopy system.[45] Figure 1b presents a room-temperature PL spectrum of a WS$_2$ monolayer centered at approximately 1.97 eV.

During the experiments, we illuminate the WS$_2$ monolayer using two linearly polarized laser beams at $\lambda_1 = 775$ nm (230 fs) and $\lambda_2 = 1200$ nm (235 fs), as shown in Figure 1a. These laser pulses are delivered by a femtosecond laser oscillator (Tsunami, Spectra-Physics) and a tunable optical parametric oscillator ($\lambda_2 = 1100−1300$ nm, OPAL, Spectra-Physics). The laser beam at 775 nm runs via a motorized linear stage to control the time delay Δt between the pulses. The pulses are recombined using a dichroic mirror and then focused at the sample surface by means of a microscope objective (Olympus UPLSAPO 40× objective, NA = 0.95), thus, achieving spatial and temporal overlap. We use an in situ optical microscope to select specific flakes and to inspect the sample surface during the experiments. The light emitted from the WS$_2$ flake is collected by the objective and imaged both at the slit of a spectrometer (Princeton Instruments, Acton, Spectra Pro 2300I) and at the chip of a CCD camera. Note that we use two concatenated low-pass filters (430 nm $< \lambda <$ 650 nm, FES0650) and a dichroic mirror (cut-on wavelength 650 nm) to filter out the fundamental infrared wavelengths λ_1 and λ_2, while being able to detect the light emitted in the visible/ultraviolet spectral range.

RESULTS AND DISCUSSIONS

In Figure 1c we present emission spectra from the excited monolayer for three illumination conditions: ω_2-only (green), ω_1, and ω_2 together without (orange) and with (blue)

temporal overlap, respectively. Note that the individual laser pulse energies are kept constant, irrespective of the illumination configuration. For the wavelength range under investigation, illumination with ω_2-only leads to SHG and degenerate two-photon PL (green curve). Illumination with ω_1 and ω_2 laser pulses, at a time delay of $\Delta t = 0$, results in four emission peaks generated via SFG, FWM, SHG, and PL (blue line). In contrast, the same illumination arrangement, with a $\Delta t = 600$ fs, shows the spectral peaks corresponding to SHG and PL and a highly diminished SFG peak (orange line). The second-order surface conductivity $\sigma^{(2)}$ mediates the generation of nonlinear sheet currents, resulting in SHG and SFG at $2\omega_2$ and $\omega_1 + \omega_2$, which we observe around 600 and 471 nm, respectively. The third-order surface conductivity $\sigma^{(3)}$ gives rise to FWM at $2\omega_1 - \omega_2$ and $2\omega_2 - \omega_1$, as shown at 572 nm (the peak at 2657 nm is not measured). Table 1 summarizes the

Table 1. Nonlinear Optical Processes at WS$_2$

process	frequency ω_{NL}	sheet current
SHG	$2\omega_2$ (600 nm)	$j^{(2)} = \sigma^{(2)}E(\omega_2)E(\omega_2)$
SFG	$\omega_1 + \omega_2$ (471 nm)	$j^{(2)} = \sigma^{(2)}E(\omega_1)E(\omega_2)$
FWM	$2\omega_1 - \omega_2$ (572 nm)	$j^{(3)} = \sigma^{(3)}E(\omega_1)E(\omega_1)E(\omega_2)$

nonlinear processes relevant to this study and the frequencies that we observe experimentally. The equations in Table 1 provide a way to distinguish the role and order of different nonlinear processes on the WS$_2$ monolayer.[12,46] We also measure a broad PL emission peak near the A-exciton frequency ($\lambda_e \approx 625$ nm), which is characteristic of a WS$_2$ monolayer, as shown in Figure 1b. The origin of PL here is exclusively nonlinear since both of the laser photon energies, $\hbar\omega_1 = 1.6$ eV and $\hbar\omega_2 = 1.0$ eV, are below the optical bandgap (≈ 1.94 eV).[47,48] In a nonparametric process like nonlinear PL, multiphoton absorption can lead to excited electrons via degenerate or nondegenerate excitation channels. After laser excitation, the excited electrons undergo a fast nonradiative relaxation to a lower energy state (i.e., excitonic ground state) and subsequently emit a photon that we identify as nonlinear PL in our spectra. We use the data acquired with the three illumination conditions in Figure 1c to elucidate which of the multiphoton excitation channels presented in the second column of Table 1 are responsible for the nonlinear exciton PL.

The PL emission obtained using (i) ω_2-only and (ii) ω_1 and ω_2 with $\Delta t = 600$ fs can exclusively be attributed to degenerate two-photon absorption mechanisms. The green-colored area corresponds to PL generated via $2\omega_2$PL (see green label), whereas the orange area that is visible on the graph (see orange label) accounts for the contribution due to $2\omega_1$PL. Consequently, the PL emission peak is more intense when exciting with ω_1, ω_2, and $\Delta t = 600$ fs, where both $2\omega_1$ and $2\omega_2$ combine to produce a two-photon PL (without any degenerate contribution). Interestingly, the blue spectrum illustrates that the PL emission doubles when the time-delay is set to zero, that is, the blue area. This increase could tentatively be attributed to the generation of excitons following $\omega_1 + \omega_2$ and $2\omega_1 - \omega_2$ multiphoton absorption pathways. Still, to be able to confirm its precise source and the order of the corresponding nonlinearity, we need to individually investigate the relation between the nonlinear PL emission and the rest of non-linearities as a function of the laser energy.

We first focus on the nonlinear optical response upon single monochromatic light illumination with ω_2. We show the energy dependence of the SHG intensity ($2\omega_2$) in Figure 2a.
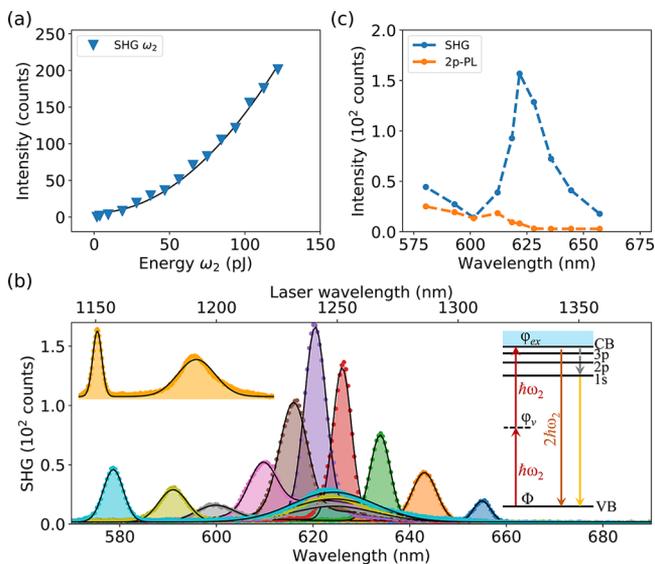
Figure 2. (a) SHG ($2\omega_2$) at 600 nm as a function of the laser pulse energy with $\lambda_2 = 1200$ nm. (b) Emission spectra obtained upon illumination using several excitation wavelengths, which are shown in the upper x-axis. All spectra in (b) were measured using an average power of 8 mW and a repetition rate of 82 MHz. The inset on the right-hand side of (b) illustrates a schematic of the SHG and $2\omega_2$PL mechanisms using an energy level diagram, where CB and VB corresponds to the conduction band and valence band, respectively. The 1s, 2p, and 3p excitonic states correspond to the energies 2.05, 2.28, and 2.49 eV computed in ref 49. (c) SHG and PL intensity as a function of wavelength ($\lambda_2/2$). To disentangle the relative contributions of the SHG and PL, we performed a double Gaussian fit to the spectra in (b) (see black solid lines and inset in (b)) to obtain the data in (c). We kept the same width and central peak for the PL signal while finding the best fit for the width and peak position of the SHG. The solid lines illustrate the fits.

The experimental data (blue triangles) illustrate a quadratic response that we confirm by fitting a second-order monomial function similar to the SHG formula in Table 1 (solid line). In order to probe the influence of the exciton at 625 nm on the nonlinear response, we also study the SHG and the $2\omega_2$PL obtained with several independent laser excitation wavelengths. During the experiment, we illuminated the monolayer with one laser beam at a time with wavelengths that range from 1150 to 1320 nm; thus, the second harmonic ranges from 575 to 660 nm, as shown by the spectra depicted in Figure 2b. The energy per pulse was set to be the same irrespective of the wavelength. To retrieve the information on the SHG and PL signals, we fit a double Gaussian function (see solid black lines) to the experimental data, as illustrated in the inset. The graph in Figure 2c depicts the peak intensity of the two-photon PL (orange) and SHG (blue) extracted from the fits. We observe a flat response of the two-photon PL signal around the 1s A-exciton, that is slightly larger when $\lambda_{SHG} < 625$ nm. On the other hand, both the spectra in Figure 2b and the graph in Figure 2c clearly illustrate an enhanced SHG emission I_{SHG} when the harmonic is in resonance with the A-exciton at 625 nm, leading to an enhancement factor of $\eta = I^{max}/I^{min} \approx 11$ at 625 nm. The origin of this enhancement can be understood by

using the microscopic theory mentioned in the introduction that describes the second-order surface conductivity $\sigma^{(2)}$ taking into account the contribution of excitons.[13,44]

To explain the SHG and two-photon PL mechanisms, we use the energy level diagram depicted in the inset of Figure 2b. The states in the diagram correspond to the ground state $|\Phi\rangle$ (i.e., top of valence band of WS$_2$), an intermediate virtual state $|\varphi_v\rangle$ and an excitonic state $|\varphi_{ex}\rangle$. According to the schematic, two laser photons with energy $\hbar\omega_2$ interact with the monolayer, and subsequently, either one photon with frequency $2\omega_2$ is emitted via SHG or a photon with frequency ω_e that corresponds to the 1s A-exciton state is emitted (i.e., PL at 625 nm). It is important to note here that SHG is a parametric process, whereas $2\omega_2$PL is a nonparametric process where two photons excite an electron that decays to the exciton ground state and emits a photon via recombination. These transitions can be formally described in terms of the surface conductivity by following Lafrentz et al.[44] and Wang et al.[13] The matrix element of the second-order surface conductivity $\sigma_{ijk}^{(2)}(2\omega_2, \omega_2, \omega_2)$ that mediates the SHG process can be written as

$$\sigma_{ijk}^{(2)} \propto 2\omega_2 d \frac{\langle\Phi|\hat{V}_i^{2\omega_2}|\varphi_{ex}\rangle}{E_{ex} - 2\hbar\omega_2 - i\Gamma_{ex}} \sum_v \frac{\langle\varphi_{ex}|\hat{V}_j^{\omega_2}|\varphi_v\rangle\langle\varphi_v|\hat{V}_k^{\omega_2}|\Phi\rangle}{E_v - \hbar\omega_2 - i\Gamma_v}$$

(1)

where the excited and virtual states correspond to energies E_{ex} and E_v, respectively, with damping rates Γ_{ex} and Γ_v, and d corresponds to the effective thickness of the monolayer. The damping rates are inversely proportional to the scattering times of each state: $\tau_{ex} = \Gamma_{ex}^{-1}$ and $\tau_v = \Gamma_v^{-1}$. The fact that the excited state $|\varphi_{ex}\rangle$ is an excitonic state makes the first term of the matrix element, that is, $\sigma^{(2)} \propto \langle\Phi|\hat{V}_i^{2\omega}|\varphi_{ex}\rangle/(E_e - 2\hbar\omega - i\Gamma_{ex})$, dominant over the terms that involve virtual states. This is mainly due to the significantly lower damping rate Γ_{ex} of an exciton generated via two-photon absorption when compared to that one Γ_v of a short-lived virtual state (i.e., $\tau_{ex} \gg \tau_v$), which consequently enhances the nonlinear optical response. The photon–exciton interaction can be accounted for using perturbation theory to expand $\hat{V}_i^{2\omega}$ up to a second-order.[44] Using the expansion of $\hat{V}_i^{2\omega}$, the SHG enhancement can be explained through an efficient combination of complementary electric and magnetic dipole transitions, as reported by Wang et al. in WSe$_2$ at cryogenic temperatures.[13] The above-mentioned understanding of the SHG process helps to understand more complex photon–exciton interactions when simultaneously exciting TMDs with several laser photon energies, that is, SFG and FWM that we show next.

Figure 3a,b depicts graphs of the intensity of the generated SFG and FWM signals as a function of the laser pulse energy for ω_1 (left) and ω_2 (right). The color markers represent the experimental data and the dashed and solid black lines are fits to linear and quadratic monomial functions, respectively. Figure 3a confirms the linear dependence of the SFG as a function of the laser energy at both frequencies. Figure 3b illustrates the quadratic (linear) energy dependence of the FWM intensity for ω_1 (ω_2).

In order to further investigate the role of nonlinear excitation channels (other than SHG) on the nonlinearly generated exciton PL, we now study the energy dependence of PL and its relation with the SFG and FWM signals. We define here the PL* as the PL signal that corresponds to the visible blue area in Figure 1c. This is the result of subtracting the
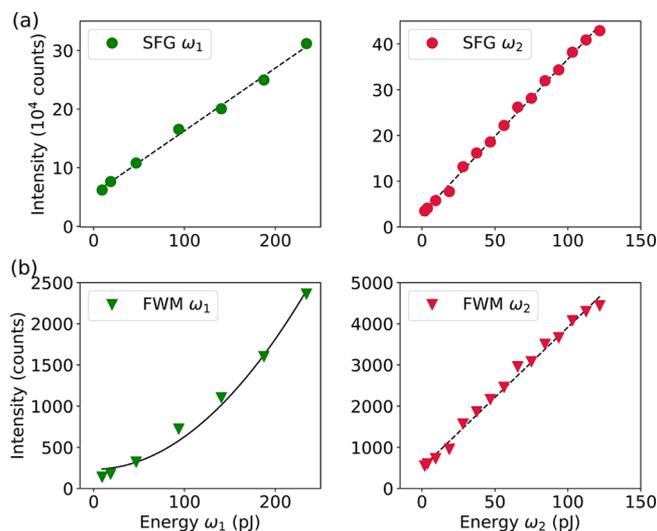
Figure 3. (a) SFG and (b) FWM signals as a function of the laser energy per pulse for ω_1 (left) and ω_2 (right). The energies of the beams at ω_1 in (b) and ω_2 in (a) correspond to 328 and 93 pJ at a repetition rate of 82 MHz. The data in the graphs correspond to the peak values extracted from the spectra at each excitation energy.

$2\omega_1$PL and $2\omega_2$PL integrated signals (orange and green visible areas in Figure 1c) from the total PL signal obtained while simultaneously ($\Delta t = 0$) exciting the sample with both photon frequencies. Therefore, PL* accounts exclusively for non-degenerate nonlinear PL, which originates as a result of excitation pathways, where ω_1 and ω_2 are combined through $\omega_1 + \omega_2$ and $2\omega_1 - \omega_2$, but not via $2\omega_1$ and $2\omega_2$. We depict the PL* intensity as a function of the laser pulse energy for ω_1 (green markers) and ω_2 (red markers) in Figure 4a. The PL* data illustrate a linear dependence with the laser energy, which is indicative of a dominance of the one-photon absorption contribution for each independent frequency or a preferred $\omega_1 + \omega_2$ degenerated excitation route. Moreover, the lack of a PL* quadratic scaling with the energy of the beam at ω_1 suggests a minimal implication of $2\omega_1 - \omega_2$ excitation route on the PL emission.

The graphs in Figure 4b,c depict the SFG signal (data in Figure 3a) against the nondegenerate PL* signal (data in Figure 4a). The data in Figure 4b (Figure 4c) were acquired keeping the energy of the laser beam at ω_2 (ω_1) constant, while increasing the energy of the beam at ω_1 (ω_2). We find a clear linear correlation between PL* and SFG, irrespective of the excitation frequency, which suggests that these processes share the same order nonlinearity. Analogously, the insets of Figure 4b,c depict the FWM signal (data in Figure 3b) against the nondegenerate PL* signal (data in Figure 4a). The FWM versus PL* signals illustrate a quadratic and linear behavior for ω_1 and ω_2, respectively. This indicates that the FWM emission is of the same order of nonlinearity as the PL* signal for ω_2, but of a higher order nonlinearity for ω_1. Furthermore, the result of these correlations points out that the nondegenerate PL* signal originates mainly via the $\omega_1 + \omega_2$ excitation route. The schematics of the energy levels in Figure 4c summarize the nonlinear processes and the PL* emission assisted via $\omega_1 + \omega_2$ and $2\omega_1 - \omega_2$ multiphoton absorption. SFG mechanism follows a two-photon excitation route similar to SHG but including two possible intermediate virtual energy levels (i.e., nondegenerate process) corresponding to $\hbar\omega_1$ and $\hbar\omega_2$. For the parametric process, two photons combine to generate a
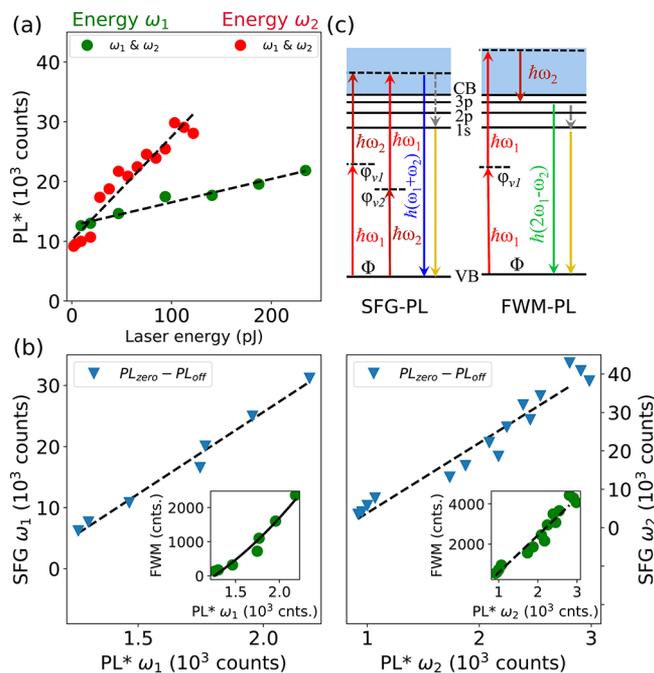
Figure 4. (a) Nonlinear PL* intensity as a function of laser energy at ω_1 (green) and ω_2 (red). (b) Graphs of the SFG signal as a function of the PL* signal on a WS_2 layer. The insets show the FWM signal as a function of the PL*. Note that the PL* intensity was calculated by subtracting the degenerate two-photon PL to the total PL. Therefore, PL* accounts exclusively for nondegenerate PL. In (a) and (b) the energies of the beams at ω_1 and ω_2 correspond to 328 pJ and 93 pJ at a repetition rate of 82 MHz. (c) Schematics of the energy levels for SFG and FWM processes. CB and VB correspond to the conduction band and valence band and 1s, 2p, and 3p excitonic states correspond to the energies 2.05, 2.28, and 2.49 eV reported in ref 49.

new photon via SFG. For the nonparametric process, two photons with frequencies $\omega_1 + \omega_2$ excite an electron that decays to the ground excitonic state that subsequently emits a photon as shown in the left diagram in Figure 4c. Analogously, the diagram on the right-hand side in Figure 4c shows the FWM mechanism and the $2\omega_1 - \omega_2$ assisted PL. The FWM generates via $2\hbar\omega_1 - \hbar\omega_2$.

CONCLUSIONS

In summary, we have investigated the nonlinear optical response of WS_2 monolayers using a multiwavelength illumination scheme. We observe and discriminate the individual influence of the degenerate and nondegenerate multiphoton absorption routes on the PL emission. We observe and explain the SHG enhancement around the 1s A-exciton of WS_2 at room temperature. We confirm the order of the nonlinear mechanisms by measuring the energy dependence of each spectral peak. Moreover, we find a linear and nonlinear correlation between PL and SFG and FWM, respectively. This reveals that $\omega_1 + \omega_2$ corresponds to the preferred nondegenerate excitation pathway of excitons over $2\omega_1 - \omega_2$. Finally, we propose that multiwavelength-based nonlinear PL, in resonance with individual excitonic states in TMDs, can be used as a sensitive observable to investigate the fast and ultrafast dynamics of excitons, which serves as an alternative route to Kerr rotation and time-resolved (linear) PL schemes. From an applied point of view, studying the influence of strain on the nonlinear response of TMD monolayers[37] by

monitoring several nonlinear effects has the potential for making progress on the fabrication of flexible photonic devices.

AUTHOR INFORMATION

Corresponding Author

L. Kuipers — *Department of Quantum Nanoscience, Kavli Institute of Nanoscience Delft, Delft University of Technology, 2628 CJ Delft, The Netherlands;* orcid.org/0000-0003-0556-8167; Email: l.kuipers@tudelft.nl

Authors

Javier Hernandez-Rueda — *Department of Quantum Nanoscience, Kavli Institute of Nanoscience Delft, Delft University of Technology, 2628 CJ Delft, The Netherlands;* orcid.org/0000-0002-8723-4832

Marc L. Noordam — *Department of Quantum Nanoscience, Kavli Institute of Nanoscience Delft, Delft University of Technology, 2628 CJ Delft, The Netherlands*

Irina Komen — *Department of Quantum Nanoscience, Kavli Institute of Nanoscience Delft, Delft University of Technology, 2628 CJ Delft, The Netherlands;* orcid.org/0000-0001-6805-090X

Complete contact information is available at:
https://pubs.acs.org/10.1021/acsphotonics.0c01567

Notes

The authors declare no competing financial interest.

REFERENCES

(1) Geim, A. K.; Novoselov, K. S. The Rise of Graphene. *Nanoscience and Technology* **2009**, 11−19.

(2) Jin, C.; Lin, F.; Suenaga, K.; Iijima, S. Fabrication of a Freestanding Boron Nitride Single Layer and Its Defect Assignments. *Phys. Rev. Lett.* **2009**, *102*, 195505.

(3) Ci, L.; Song, L.; Jin, C.; Jariwala, D.; Wu, D.; Li, Y.; Srivastava, A.; Wang, Z.; Storr, K.; Balicas, L.; et al. Atomic layers of hybridized boron nitride and graphene domains. *Nat. Mater.* **2010**, *9*, 430.

(4) Bonaccorso, F.; Sun, Z.; Hasan, T.; Ferrari, A. Graphene photonics and optoelectronics. *Nat. Photonics* **2010**, *4*, 611.

(5) Sun, Z.; Martinez, A.; Wang, F. Optical modulators with 2D layered materials. *Nat. Photonics* **2016**, *10*, 227.

(6) Gong, S.-H.; Alpeggiani, F.; Sciacca, B.; Garnett, E. C.; Kuipers, L. Nanoscale chiral valley-photon interface through optical spin-orbit coupling. *Science* **2018**, *359*, 443−447.

(7) Noori, Y. J.; Cao, Y.; Roberts, J.; Woodhead, C.; Bernardo-Gavito, R.; Tovee, P.; Young, R. J. Photonic crystals for enhanced light extraction from 2D materials. *ACS Photonics* **2016**, *3*, 2515−2520.

(8) Palacios, E.; Park, S.; Lauhon, L.; Aydin, K. Identifying excitation and emission rate contributions to plasmon-enhanced photoluminescence from monolayer MoS2 using a tapered gold nanoantenna. *ACS Photonics* **2017**, *4*, 1602−1606.

(9) Huang, W.; De-Eknamkul, C.; Zhang, X.; Leewong, E.; Zhao, M.-Q.; Johnson, A. C.; Cubukcu, E. Monolayer Excitonic Emission for Imaging Spatial Dispersion of Photonic Crystals. *ACS Photonics* **2019**, *6*, 2312−2319.

(10) Jariwala, D.; Davoyan, A. R.; Wong, J.; Atwater, H. A. Van der Waals materials for atomically-thin photovoltaics: Promise and outlook. *ACS Photonics* **2017**, *4*, 2962−2970.

(11) Gan, L.-Y.; Zhang, Q.; Cheng, Y.; Schwingenschlogl, U. Photovoltaic heterojunctions of fullerenes with MoS2 and WS2 monolayers. *J. Phys. Chem. Lett.* **2014**, *5*, 1445−1449.

(12) Hendry, E.; Hale, P. J.; Moger, J.; Savchenko, A. K.; Mikhailov, S. A. Coherent Nonlinear Optical Response of Graphene. *Phys. Rev. Lett.* **2010**, *105*, 097401.

(13) Wang, G.; Marie, X.; Gerber, I.; Amand, T.; Lagarde, D.; Bouet, L.; Vidal, M.; Balocchi, A.; Urbaszek, B. Giant Enhancement of the Optical Second-Harmonic Emission of WSe$_2$ Monolayers by Laser Excitation at Exciton Resonances. *Phys. Rev. Lett.* **2015**, *114*, 097403.

(14) Dean, J. J.; van Driel, H. M. Second harmonic generation from graphene and graphitic films. *Appl. Phys. Lett.* **2009**, *95*, 261910.

(15) Autere, A.; Jussila, H.; Dai, Y.; Wang, Y.; Lipsanen, H.; Sun, Z. Nonlinear Optics with 2D Layered Materials. *Adv. Mater.* **2018**, *30*, 1705963.

(16) Malard, L. M.; Alencar, T. V.; Barboza, A. P. M.; Mak, K. F.; de Paula, A. M. Observation of intense second harmonic generation from MoS_2 atomic crystals. *Phys. Rev. B: Condens. Matter Mater. Phys.* **2013**, *87*, 201401.

(17) Kumar, N.; Najmaei, S.; Cui, Q.; Ceballos, F.; Ajayan, P. M.; Lou, J.; Zhao, H. Second harmonic microscopy of monolayer MoS_2. *Phys. Rev. B: Condens. Matter Mater. Phys.* **2013**, *87*, 161403.

(18) Li, Y.; Rao, Y.; Mak, K. F.; You, Y.; Wang, S.; Dean, C. R.; Heinz, T. F. Probing Symmetry Properties of Few-Layer MoS_2 and h-BN by Optical Second-Harmonic Generation. *Nano Lett.* **2013**, *13*, 3329−3333.

(19) Hsu, W.-T.; Zhao, Z.-A.; Li, L.-J.; Chen, C.-H.; Chiu, M.-H.; Chang, P.-S.; Chou, Y.-C.; Chang, W.-H. Second Harmonic Generation from Artificially Stacked Transition Metal Dichalcogenide Twisted Bilayers. *ACS Nano* **2014**, *8*, 2951−2958.

(20) Shi, J.; Yu, P.; Liu, F.; He, P.; Wang, R.; Qin, L.; Zhou, J.; Li, X.; Zhou, J.; Sui, X.; et al. 3R MoS_2 with broken inversion symmetry: a promising ultrathin nonlinear optical device. *Adv. Mater.* **2017**, *29*, 1701486.

(21) Woodward, R. I.; Murray, R. T.; Phelan, C. F.; de Oliveira, R. E. P.; Runcorn, T. H.; Kelleher, E. J. R.; Li, S.; de Oliveira, E. C.; Fechine, G. J. M.; Eda, G.; de Matos, C. J. S. Characterization of the second- and third-order nonlinear optical susceptibilities of monolayer MoS$_2$ using multiphoton microscopy. *2D Mater.* **2017**, *4*, 011006.

(22) Säynätjoki, A.; et al. Ultra-strong nonlinear optical processes and trigonal warping in MoS$_2$ layers. *Nat. Commun.* **2017**, *8*, 1−8.

(23) Le, C. T.; Clark, D. J.; Ullah, F.; Senthilkumar, V.; Jang, J. I.; Sim, Y.; Seong, M.-J.; Chung, K.-H.; Park, H.; Kim, Y. S. Nonlinear optical characteristics of monolayer $MoSe_2$. *Ann. Phys.* **2016**, *528*, 551−559.

(24) Autere, A.; Jussila, H.; Marini, A.; Saavedra, J. R. M.; Dai, Y.; Säynätjoki, A.; Karvonen, L.; Yang, H.; Amirsolaimani, B.; Norwood, R. A.; Peyghambarian, N.; Lipsanen, H.; Kieu, K.; de Abajo, F. J. G.; Sun, Z. Optical harmonic generation in monolayer group-VI transition metal dichalcogenides. *Phys. Rev. B: Condens. Matter Mater. Phys.* **2018**, *98*, 115426.

(25) Beams, R.; Cançado, L. G.; Krylyuk, S.; Kalish, I.; Kalanyan, B.; Singh, A. K.; Choudhary, K.; Bruma, A.; Vora, P. M.; Tavazza, F.; Davydov, A. V.; Stranick, S. J. Characterization of Few-Layer 1T $MoTe_2$ by Polarization-Resolved Second Harmonic Generation and Raman Scattering. *ACS Nano* **2016**, *10*, 9626−9636.

(26) Ribeiro-Soares, J.; Janisch, C.; Liu, Z.; Elias, A. L.; Dresselhaus, M. S.; Terrones, M.; Cançado, L. G.; Jorio, A. Second Harmonic Generation in WSe2. *2D Mater.* **2015**, *2*, 045015.

(27) Janisch, C.; Mehta, N.; Ma, D.; Elías, A. L.; Perea-López, N.; Terrones, M.; Liu, Z. Ultrashort optical pulse characterization using WS_2 monolayers. *Opt. Lett.* **2014**, *39*, 383−385.

(28) Janisch, C.; Wang, Y.; Ma, D.; Mehta, N.; Elías, A. L.; Perea-López, N.; Terrones, M.; Crespi, V.; Liu, Z. Extraordinary second harmonic generation in tungsten disulfide monolayers. *Sci. Rep.* **2015**, *4*, 5530.

(29) Cui, Q.; Muniz, R. A.; Sipe, J. E.; Zhao, H. Strong and anisotropic third-harmonic generation in monolayer and multilayer ReS$_2$. *Phys. Rev. B: Condens. Matter Mater. Phys.* **2017**, *95*, 165406.

(30) Li, D.; Xiong, W.; Jiang, L.; Xiao, Z.; Rabiee Golgir, H.; Wang, M.; Huang, X.; Zhou, Y.; Lin, Z.; Song, J.; Ducharme, S.; Jiang, L.; Silvain, J.-F.; Lu, Y. Multimodal Nonlinear Optical Imaging of MoS_2 and MoS_2-Based van der Waals Heterostructures. *ACS Nano* **2016**, *10*, 3766−3775.

(31) Jakubczyk, T.; Delmonte, V.; Koperski, M.; Nogajewski, K.; Faugeras, C.; Langbein, W.; Potemski, M.; Kasprzak, J. Radiatively Limited Dephasing and Exciton Dynamics in MoSe$_2$ Monolayers Revealed with Four-Wave Mixing Microscopy. *Nano Lett.* **2016**, *16*, 5333−5339.

(32) Bolhuis, M.; Hernandez-Rueda, J.; van Heijst, S.; Rivas, M. T.; Kuipers, L.; Conesa-Boj, S. Vertically-oriented MoS 2 nanosheets for nonlinear optical devices. *Nanoscale* **2020**, *12*, 10491−10497.

(33) Dai, Y.; Wang, Y.; Das, S.; Xue, H.; Bai, X.; Hulkko, E.; Zhang, G.; Yang, X.; Dai, Q.; Sun, Z. Electrical Control of Interband Resonant Nonlinear Optics in Monolayer MoS2. *ACS Nano* **2020**, *14*, 8442−8448.

(34) Hao, K.; Moody, G.; Wu, F.; Dass, C. K.; Xu, L.; Chen, C.-H.; Sun, L.; Li, M.-Y.; Li, L.-J.; MacDonald, A. H.; Li, X.; et al. Direct measurement of exciton valley coherence in monolayer WSe$_2$. *Nat. Phys.* **2016**, *12*, 677−682.

(35) Jakubczyk, T.; Nogajewski, K.; Molas, M. R.; Bartos, M.; Langbein, W.; Potemski, M.; Kasprzak, J. Impact of environment on dynamics of exciton complexes in a WS2 monolayer. *2D Mater.* **2018**, *5*, 031007.

(36) Seyler, K. L.; Schaibley, J. R.; Gong, P.; Rivera, P.; Jones, A. M.; Wu, S.; Yan, J.; Mandrus, D. G.; Yao, W.; Xu, X. Electrical control of second-harmonic generation in a WSe 2 monolayer transistor. *Nat. Nanotechnol.* **2015**, *10*, 407−411.

(37) Mennel, L.; Furchi, M. M.; Wachter, S.; Paur, M.; Polyushkin, D. K.; Mueller, T. Optical imaging of strain in two-dimensional crystals. *Nat. Commun.* **2018**, *9*, 516.

(38) Zeng, J.; Yuan, M.; Yuan, W.; Dai, Q.; Fan, H.; Lan, S.; Tie, S. Enhanced second harmonic generation of MoS 2 layers on a thin gold film. *Nanoscale* **2015**, *7*, 13547−13553.

(39) Karvonen, L.; et al. Rapid visualization of grain boundaries in monolayer MoS$_2$ by multiphoton microscopy. *Nat. Commun.* **2017**, *8*, 1−8.

(40) Liu, Q.; Guo, B.; Rao, Z.; Zhang, B.; Gong, J. R. Strong two-photon-induced fluorescence from photostable, biocompatible nitrogen-doped graphene quantum dots for cellular and deep-tissue imaging. *Nano Lett.* **2013**, *13*, 2436−2441.

(41) Ananthanarayanan, A.; Wang, Y.; Routh, P.; Sk, M. A.; Than, A.; Lin, M.; Zhang, J.; Chen, J.; Sun, H.; Chen, P. Nitrogen and phosphorus co-doped graphene quantum dots: synthesis from adenosine triphosphate, optical properties, and cellular imaging. *Nanoscale* **2015**, *7*, 8159−8165.

(42) Lee, K.; Tian, Y.; Yang, H.; Mustonen, K.; Martinez, A.; Dai, Q.; Kauppinen, E.; Malowicki, J.; Kumar, P.; Sun, Z. Carbon Nanotubes: Photon-Pair Generation with a 100 nm Thick Carbon Nanotube Film. *Adv. Mater.* **2017**, *29*, na.

(43) Wang, F.; Dukovic, G.; Brus, L. E.; Heinz, T. F. The optical resonances in carbon nanotubes arise from excitons. *Science* **2005**, *308*, 838−841.

(44) Lafrentz, M.; Brunne, D.; Rodina, A. V.; Pavlov, V. V.; Pisarev, R. V.; Yakovlev, D. R.; Bakin, A.; Bayer, M. Second-harmonic generation spectroscopy of excitons in ZnO. *Phys. Rev. B: Condens. Matter Mater. Phys.* **2013**, *88*, 235207.

(45) Noordam, M.; Hernandez-Rueda, J.; Talsma, L.; Kuipers, L. Plasmon-induced enhancement of nonlinear optical processes in a double-resonant metallic nanostructure grating. *Appl. Phys. Lett.* **2020**, *116*, 101101.

(46) Boyd, R. W. *Nonlinear Optics*; Elsevier, 2003.

(47) Zeng, H.; et al. Optical signature of symmetry variations and spin-valley coupling in atomically thin tungsten dichalcogenides. *Sci. Rep.* **2013**, *3*, 1608.

(48) Berkdemir, A.; et al. Identification of individual and few layers of WS$_2$ using Raman spectroscopy. *Sci. Rep.* **2013**, *3*, 1755.

F

(49) Ye, Z.; Cao, T.; O'brien, K.; Zhu, H.; Yin, X.; Wang, Y.; Louie, S. G.; Zhang, X. Probing excitonic dark states in single-layer tungsten disulphide. *Nature* **2014**, *513*, 214−218.